Supporting Information for

Tunable Electrical and Optical Characteristics in Monolayer Graphene and Few-layer MoS_2 Heterostructure Devices

Servin Rathi,[†#] Inyeal Lee,[†#] Dongsuk Lim,[‡] Jianwei Wang,[†] Yuichi Ochiai,[§] Nobuyuki Aoki,[§]

Kenji Watanabe,[⊥] Takashi Taniguchi,[⊥] Gwan-Hyoung Lee,[∥] Young-Jun Yu,[¶] Philip Kim,[▽] and

*Gil-Ho Kim[†]**

[†]School of Electronic and Electrical Engineering, and Sungkyunkwan Advanced Institute of Nanotechnology (SAINT), Sungkyunkwan University, Suwon 440-746, Korea

[‡]School of Advanced Materials Science and Engineering, Sungkyunkwan University, Suwon 440-746, Korea

[§]Graduate School of Advanced Integration Science, Chiba University, 1-33 Yayoi-cho, Inage-ku, Chiba 263-8522, Japan

[⊥]Advanced Materials Laboratory, National Institute for Materials Science, 1-1 Namiki, Tsukuba, 305-0044, Japan

[∥]Department of Material Science and Engineering, Yonsei University, Seoul 120-749, Korea

[¶]Creative Research Center for Graphene Electronics and Telecommunications Research Institute (ETRI), Daejeon 305-700, Korea

[▽]Department of Physics, Harvard University, Cambridge, MA 02138, USA

Main Contents

A. Device Fabrication Procedure

For device fabrication, graphene and MoS_2 layers were exfoliated using typical scotch tape method. While graphene was exfoliated on both 90 nm and 300 nm SiO_2-Si wafer whereas MoS_2 was exfoliated on a specially prepared wafer for transfer purpose. For this, firstly a layer of water-soluble PVA (polyvinyl alcohol) soln. was spin-coated onto a clean Si wafer followed by a layer of PMMA resist. This layer system on Si wafer was then baked to 180^{o}C on a hot-plate for 2 min. After cooling down, this wafer was used to exfoliate MoS_2 layers. After marking the desired MoS_2 layer using optical microscope, the wafer was put in DI water where PVA

dissolved, leaving the PMMA layer floating in water. The suspended film was then fished out and transferred onto the desired location on the graphene layer, using a modified high resolution microscope system. The sample was then soaked in acetone for several hours to remove the PMMA, followed by a mild annealing in H_2 and N_2 at 200 ^oC in order to remove any organic impurities. Finally, connecting electrodes were patterned using electron-beam lithography followed by metal deposition and lift-off.

Figure S1 (a-c) show the schematic of the transferred exfoliated layer of the graphene and MoS_2 layers which were then patterned by Electron Beam Lithography and subsequently contacted by electron-beam metal deposition and lift-off. Figure S1 (d-e) illustrates the top and the cross-sectional view of the device, respectively. Figure S2 (a-d) show the real image of the individual exfoliated layers, transferred layers and finally the sample after e-beam patterned, metal deposition and lift-off.

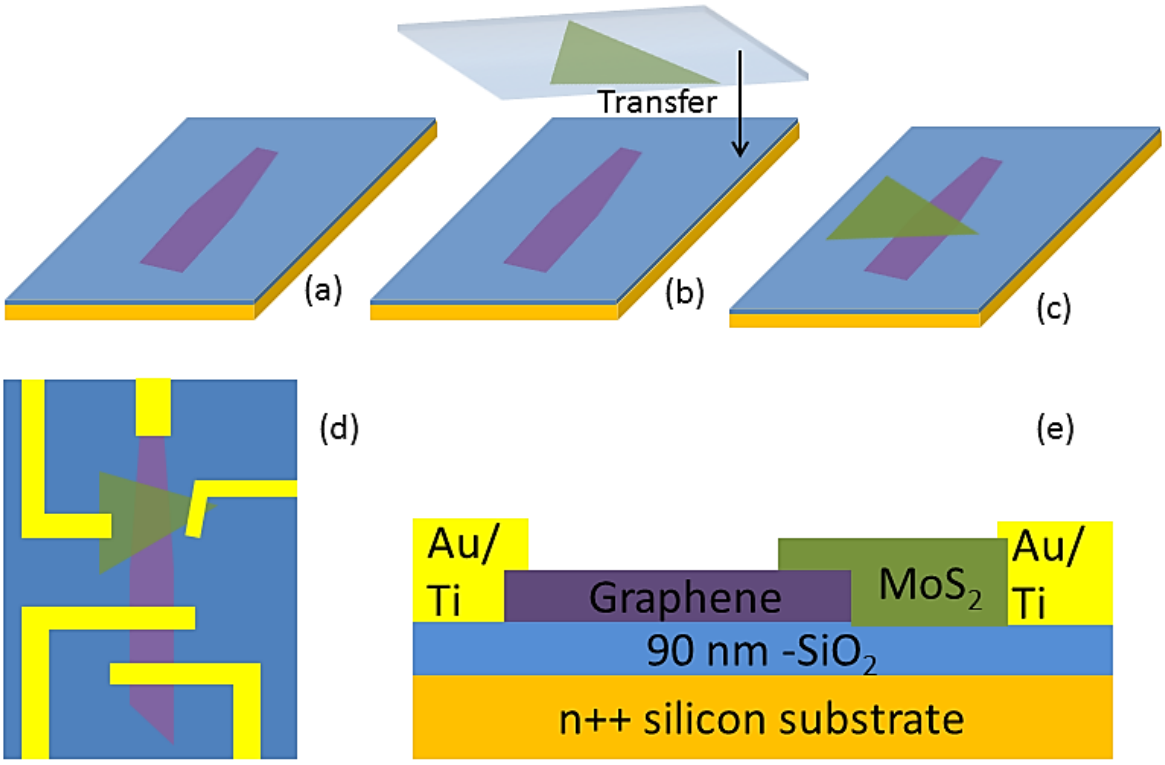

Figure S1. Schematic of layer transfer process (a)-(c) graphene and MoS_2 layer exfoliation and transfer (d) top-view and (e) cross-section view of the device after metal electrodes patterning, metal deposition and lift-off.

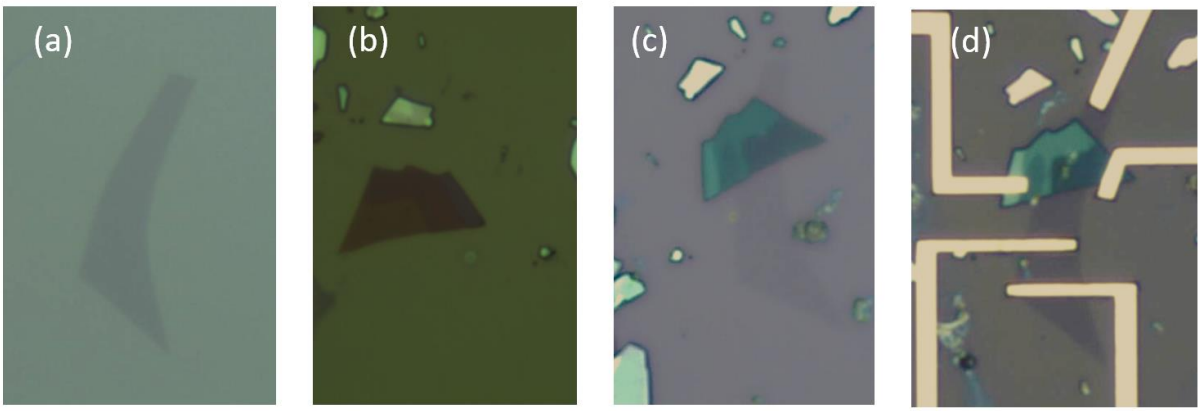

Figure S2. Optical Microscope image of the (a) single graphene (b) multi-layer MoS_2 (c) layers after transfer of MoS_2 onto graphene and (d) final device.

B. Raman Spectra of the main device

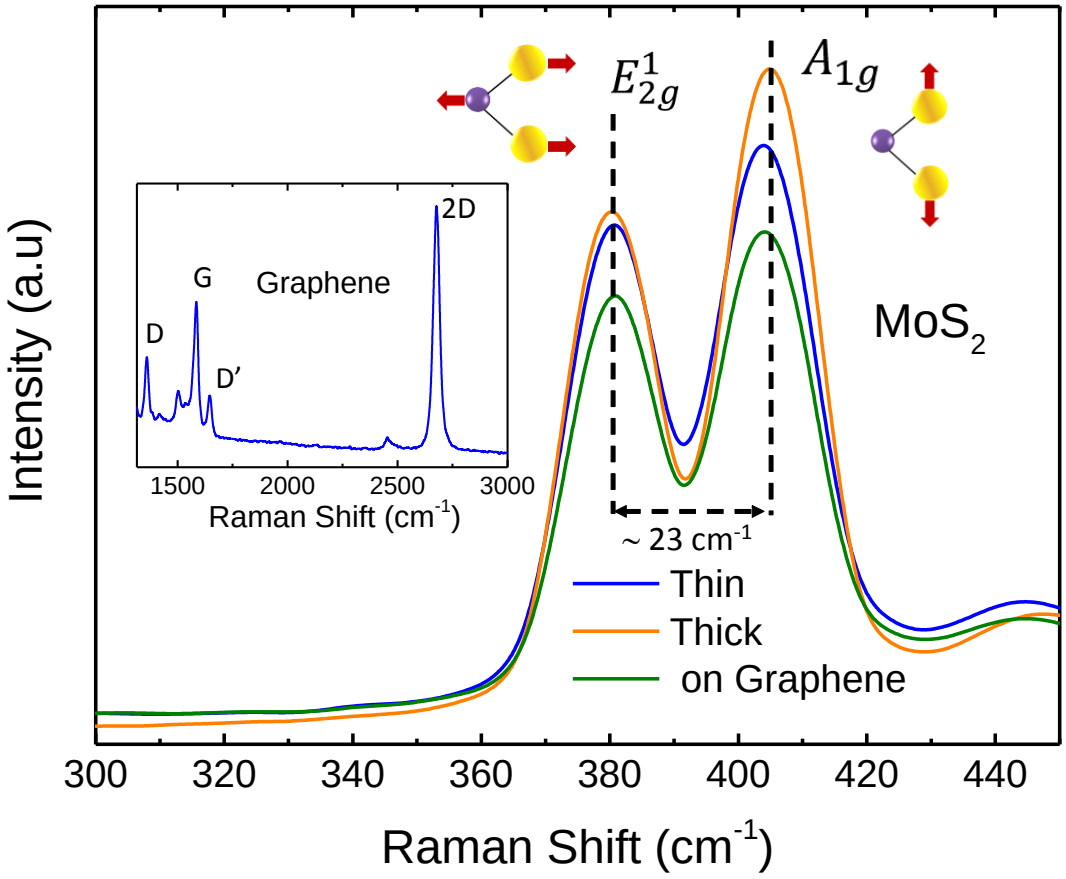

Figure S3. Raman spectra of a few layer MoS_2 with the inset showing the typical peaks of single-layer graphene.

Raman spectra of the fabricated device is shown in Figure S3 where the characteristics peaks indicates a single layer graphene and a tri-layer MoS_2.[1-3] As seen in the figure S2 the transferred MoS_2 layer seems thicker on side, the same has been found in the Raman spectra where the thinner MoS_2 layer has ≈ 23 cm^{-1} shift difference. For graphene, various peaks like D, G, D' and 2D peaks shows the typical Raman signature of a single layer graphene. Further, the quenching of MoS_2 peak intensity at the overlapped region is also observed, similar to photoluminescence,

possibly due to photo-exciton splitting at the built-in potential barrier resulting in the reduced recombination events.[4]

C. Dirac Point shift due to residual charge doping in the monolayer graphene

For this the value of the shifted Dirac point, usually on the positive gate bias is considered to derive the residual charge density using: $n_{res} = (C_{ox}V_{dirac})/q$ where for 90 and 300 nm thick SiO_2, C_{ox} is 3.83×10^{-8} and 1.15×10^{-8} F cm^{-2}, respectively. Using the derived n_{res}, the corresponding shift in the Fermi Level from the neutral point is then calculated using: $\Delta E_{Fg} = \hbar\, v_F \sqrt{\pi n_{res}}$ where ħ is Planck's constant and v_F is the Fermi velocity.[15] Almost all our samples showed the Dirac point at + 10 V for 90 nm SiO_2 which gives a downwards shift in the Fermi level by 0.18 eV approximately.

Unlike graphene, the change in the Fermi level energy in MoS_2 is almost negligible for background substrate impurities ($\Delta E_{Fm} = \pi\, \hbar^2 \Delta n/m^*$, where $m^* = 0.35m_o$ and Δn is the change in the carrier density. Therefore, MoS_2 appears to be less affected compared with graphene-based devices.

D. Electrical characteristics of the other asymmetrical contacts to MoS_2 (as seen in the Figure 1a of the main text)

As seen from the curves in the figure S4, the rectifying property can also be observed from this asymmetrical contacts, similar to the other contacts as shown in the main text. Besides measuring the conventional MoS_2 grounded state configuration, graphene grounded configuration has also been measured (Figure S4b). The band diagram in figure S4 c and d illustrate the barrier position for all the bias conditions. In figure S4c, it can be seen that for negative back-gate bias, free carriers in MoS_2 are depleted and the Fermi-level in graphene shifted downwards which resulted

in higher barrier for negative source drain bias which leads to decrease in the drain current. However for positive back-gate bias, MoS_2 is populated with high carrier density and Fermi level in graphene rises up due to electron doping by the back-gate field. This results in lowering of barrier at MoS_2-graphene contact which led to an increase in the drain current, whereas the MoS_2 barrier with metal doesn't show much variation due to relatively fixed barrier height, so the drain current at this barrier is comparatively less affected. Although, an increase in the current at this barrier with positive back-gate bias has been observed and can be explained due to a slight lowering of the effective barrier with back-gate voltage due to the increase in tunneling and thermionic field current across the barrier.

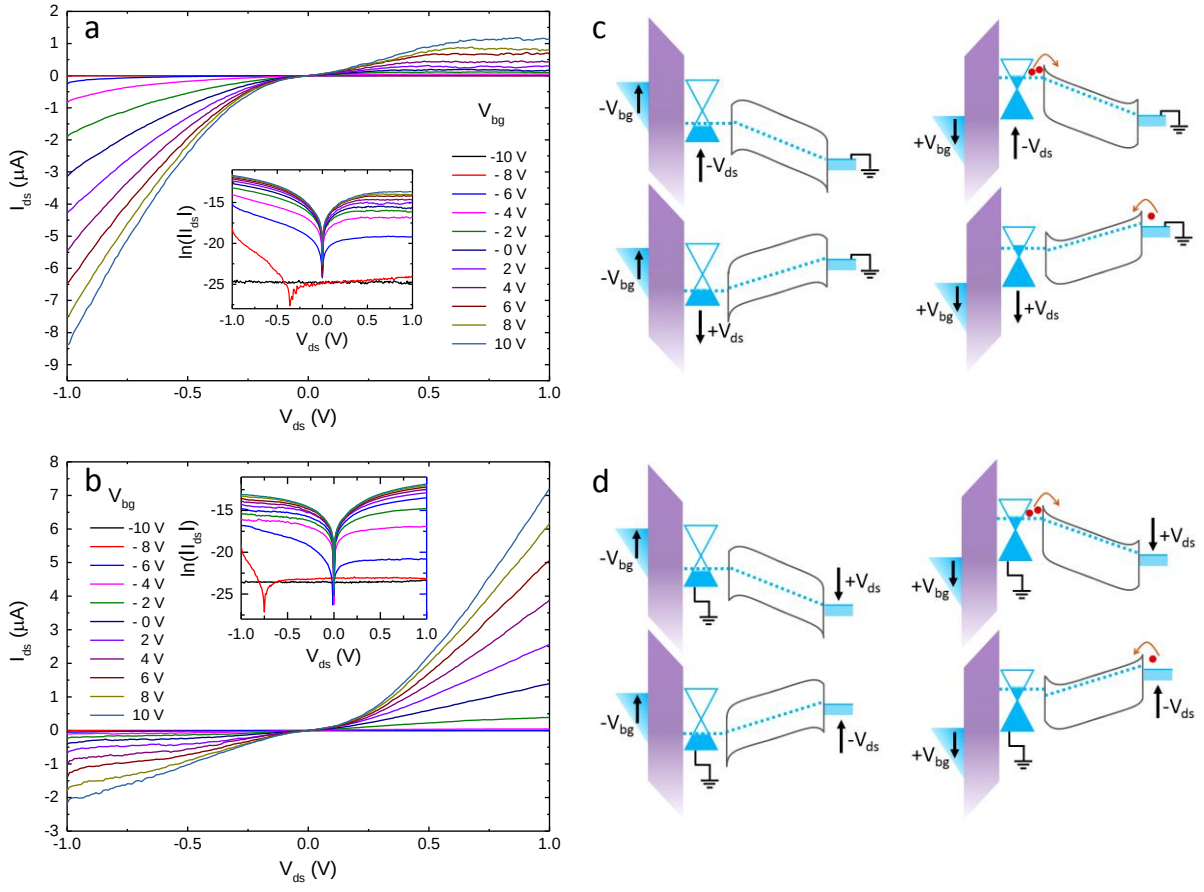

Figure. S4 Electrical characteristics of the lateral MoS_2-graphene device. (a) and (b) Current vs. drain voltage curve at various back-gate bias voltages for grounded MoS_2 and graphene contact, respectively; the insets show the semi-log curves. (c) and (d) Energy band diagrams illustrating various drain and back gate bias combinations for the curves in (a) and (b), respectively.

E. Semi-log plot of transfer characteristics as seen in Figure 3c of the main text

Figure S5 plots the current as a function of back-gate voltage for the metal connected MoS_2 FET on a semi-log scale, the inset shows the main curve on the linear scale. On/off ratio of 10^5 order is obtained along with a mobility of around 15 $cm^2/V.s$

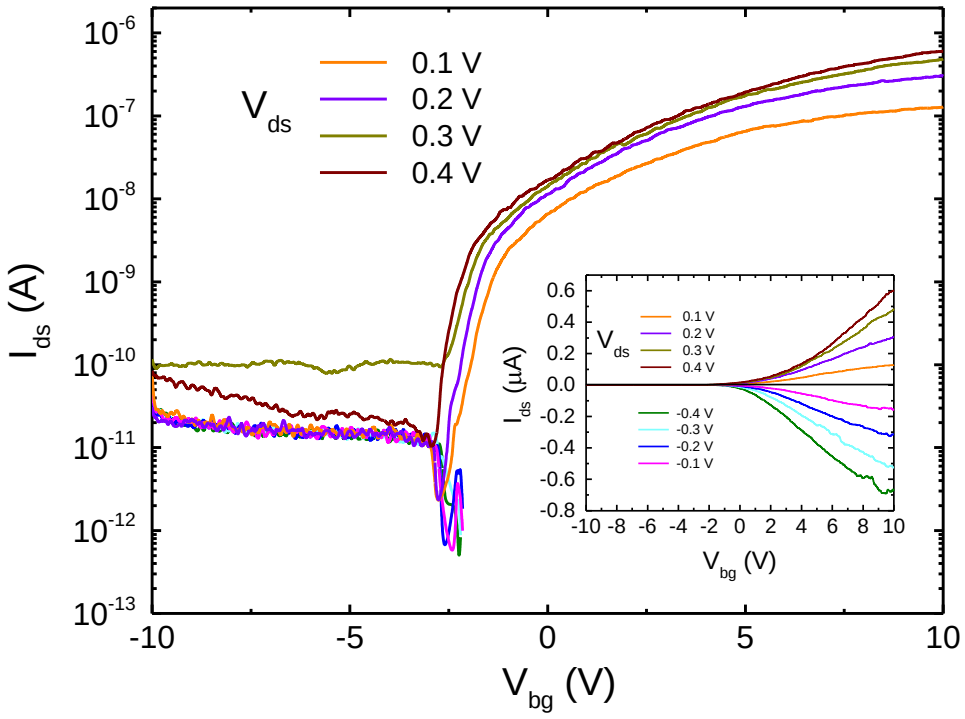

Figure. S5 Semi-log plot of transfer characteristics of the symmetrical metal contact to the MoS_2 layer for the device shown in figure 1a of the main text. The inset plots the main curve in the linear scale for both negative and positive drain bias.

F. Fitting of the rectifying curve

The metal-semiconductor diode characteristics can be modeled with the Shockley diode equation[5-8] as follows:

$$|I_{ds}| = |I_{rs}| \left(\exp\left(\frac{qV_{ds}}{nk_BT}\right) - 1\right) \quad \text{(S1a)}$$

$$I_{rs} = AA^*T^2 \exp\left(\frac{-q\phi_b}{k_BT}\right) \quad \text{(S1b)}$$

where I_{ds} is the drain current, V_{ds} is the applied voltage across junction, q is the electronic charge, n is the ideality factor, k_B is the Boltzmann constant, T is the temperature, I_{rs} is the reverse saturation current, A is the area of the Schottky junction, A* is the effective Richardson constant ($A^* = 4\pi q m^* k_B^2 h^{-3}$, where m^* is the effective mass of charge carriers in MoS_2 [9,10] and h is Planck's constant) and ϕ_b is the effective Schottky barrier height. The ideality factor, n, is derived from the slope of the $ln\left(\frac{|I_{ds}|}{|I_{rs}|} + 1\right)$ versus V_{ds} curve using the modified equation for large internal series resistance[6]:

$$|I_{ds}| = |I_{rs}| \left(\exp\left(\frac{q(V_{ds} - I_{ds}R_s}{nk_BT}\right) - 1\right). \quad \text{(S2)}$$

The best fit was obtained for resistance (R_s) ≈ 1 MΩ and an ideality factor ≈ 2.9 was obtained from the slope of the curve. The higher value of ideality factor is possibly due to the high resistance from the MoS_2 layer and barrier at the metal contact, higher recombination in space charge region, inhomogeneity in the barrier height of the graphene-MoS_2 contact due to electron-hole puddles in graphene and non-Schottky type conduction process across the

barrier.[5,10-12] Further, using the expression of the Richardson constant for $|I_{rs}| = 2.7 \times 10^{-8}$ A, the effective Schottky barrier height at the contact is calculated to be 0.34 eV, which agrees with other published results.[13-14]

G. Electrical characterization and application of other MoS_2-Graphene Hybrid Devices

Figure S6 and 7 plots the I_{ds} versus V_{ds} curve of the devices fabricated using the similar techniques. Devices shown in the inset of figure S6a and S7a were fabricated on substrate with 300 nm and 90 nm SiO_2 thickness, respectively. Rectifying behavior, well-modulated by the back gate bias, is observed in figure S6 and S7. For negative gate bias, the asymmetry in the current for positive and negative drain voltage region increases rapidly until it reaches the off state while for positive gate bias, the rectification decreases and for high positive back gate bias, ohmic-like behavior is observed.

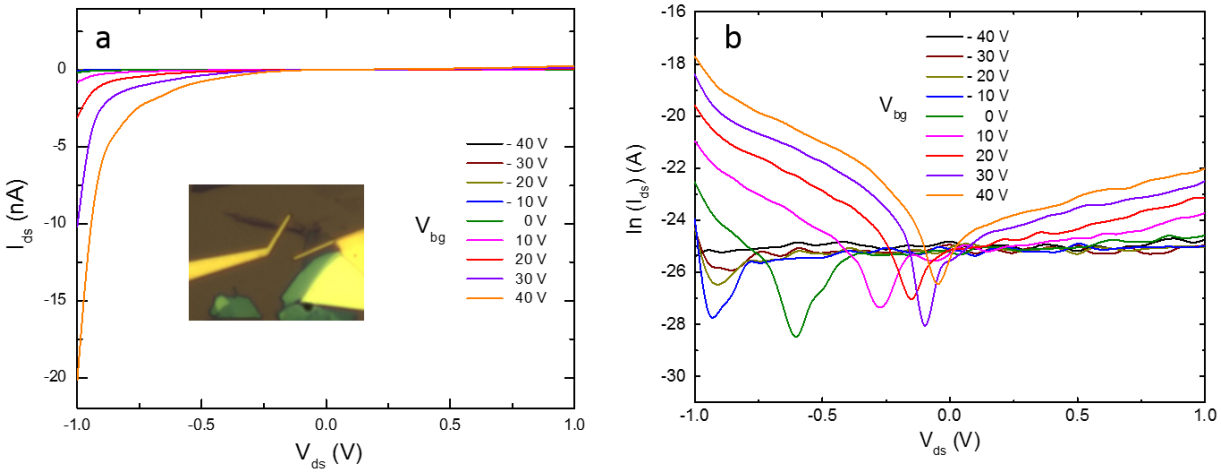

Figure. S6 (a) Current-voltage characteristics of the graphene-MoS_2 hybrid sample (shown in the inset microscopic image) at various back gate voltage (b) semi-log plot of the curves in (a).

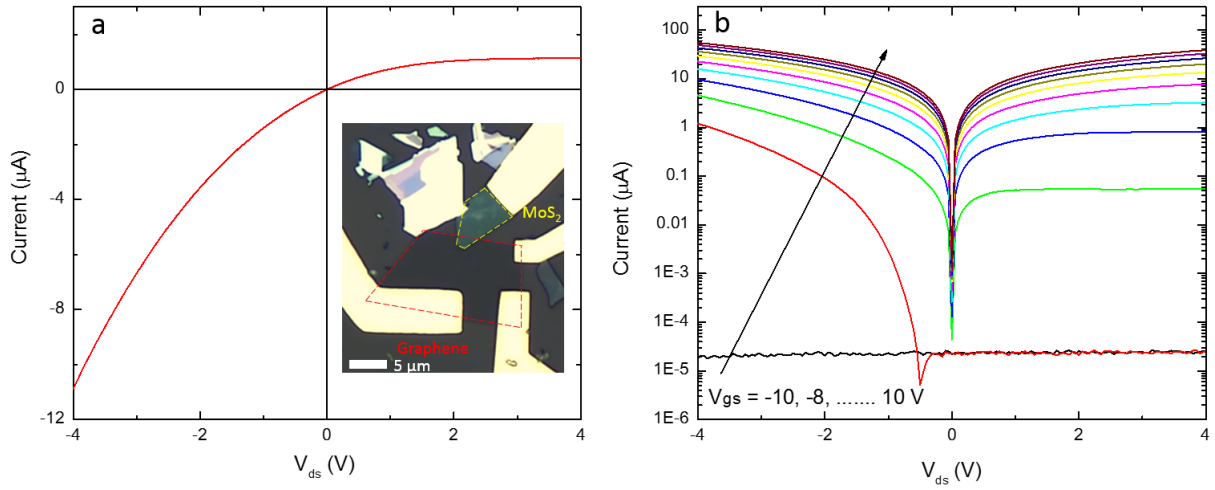

Figure. S7 (a) Current-voltage characteristics of the graphene-MoS_2 device, as shown in the inset microscopic image, for V_{gs} = 0 V (b) semi-log curve showing current-voltage curve at various gate voltages.

Figure S8 plots the transfer characteristics of the device, shown in the inset of figure S7a.

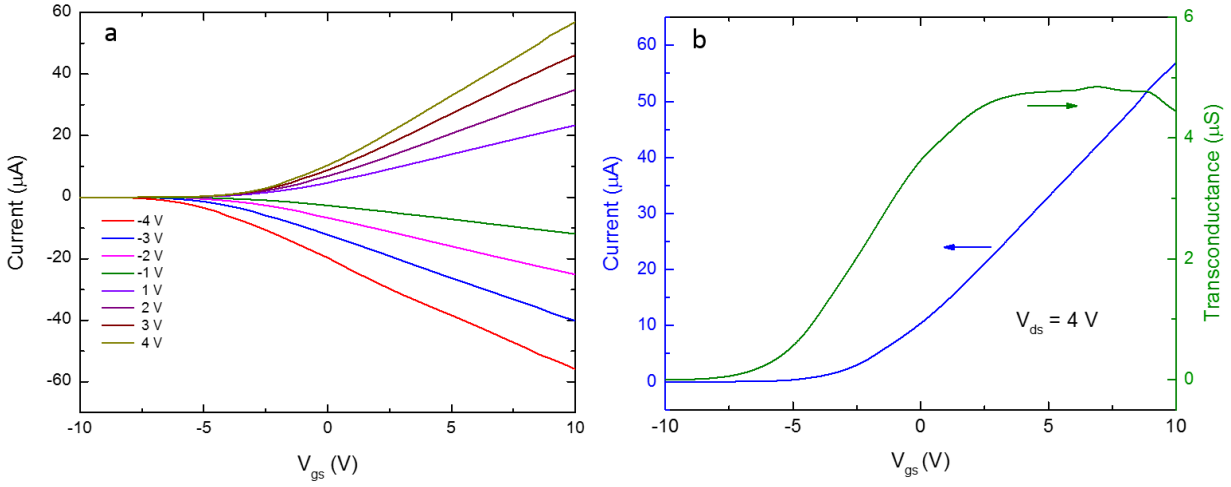

Figure. S8 (a) Transfer characteristics of the device, shown in the inset of figure S7a, at various drain voltages (b) transfer and transconductance curve at drain bias of 4 V.

Figure S9 and S10 demonstrates the application of MoS_2-graphene heterostructure devices as gate tunable diodes or barristors. It can be seen that the applied signal (sine or square wave) can be rectified, switched off or remained as it, depending on the applied gate bias. For highly positive gate bias (+10 V), the device contacts behaved as ohmic so the applied signal is passed without any rectification, though it appeared to be slightly attenuated due to voltage drop across the high series resistance of the device. However, for non-positive gate bias, device worked as diode by rectifying the signal on one half cycle and for high negative bias, the device becomes completely off (as seen in figure S8a) and no signal appeared on the output. Both sine and square wave signals (Figure S9 and S10) demonstrate this barristor type behavior where the rectification properties can be modulated by an external gate bias.

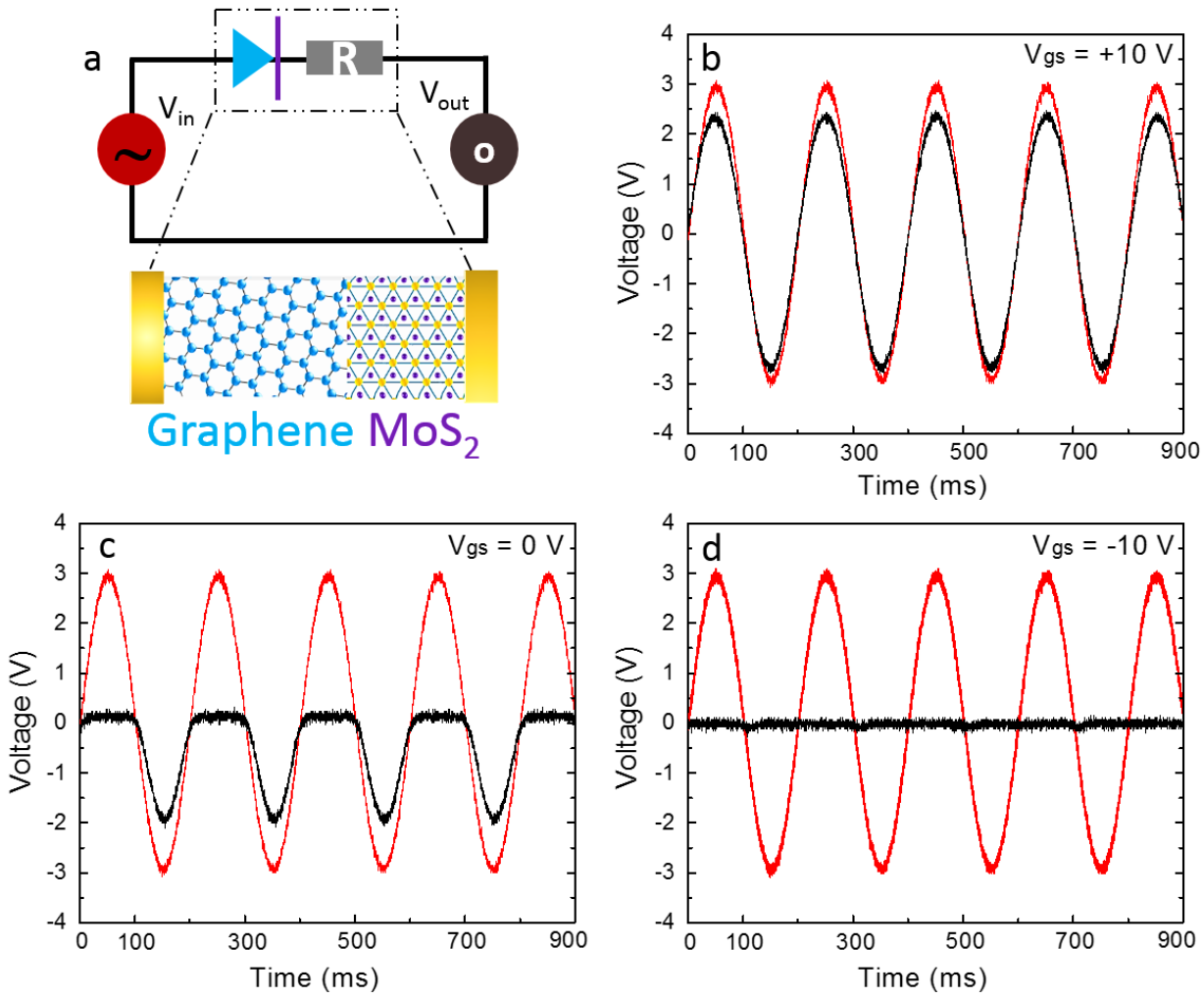

Figure. S9 (a) Schematic of the measurement set-up for rectifying sine-wave input signal. The measurement were carried out at (b) positive (V_{gs} = + 10 V) (c) neutral (V_{gs} = 0 V) and (d) negative (V_{gs} = - 10 V) gate voltages. (The red curves indicate the input signal and the black curves show the output signal)

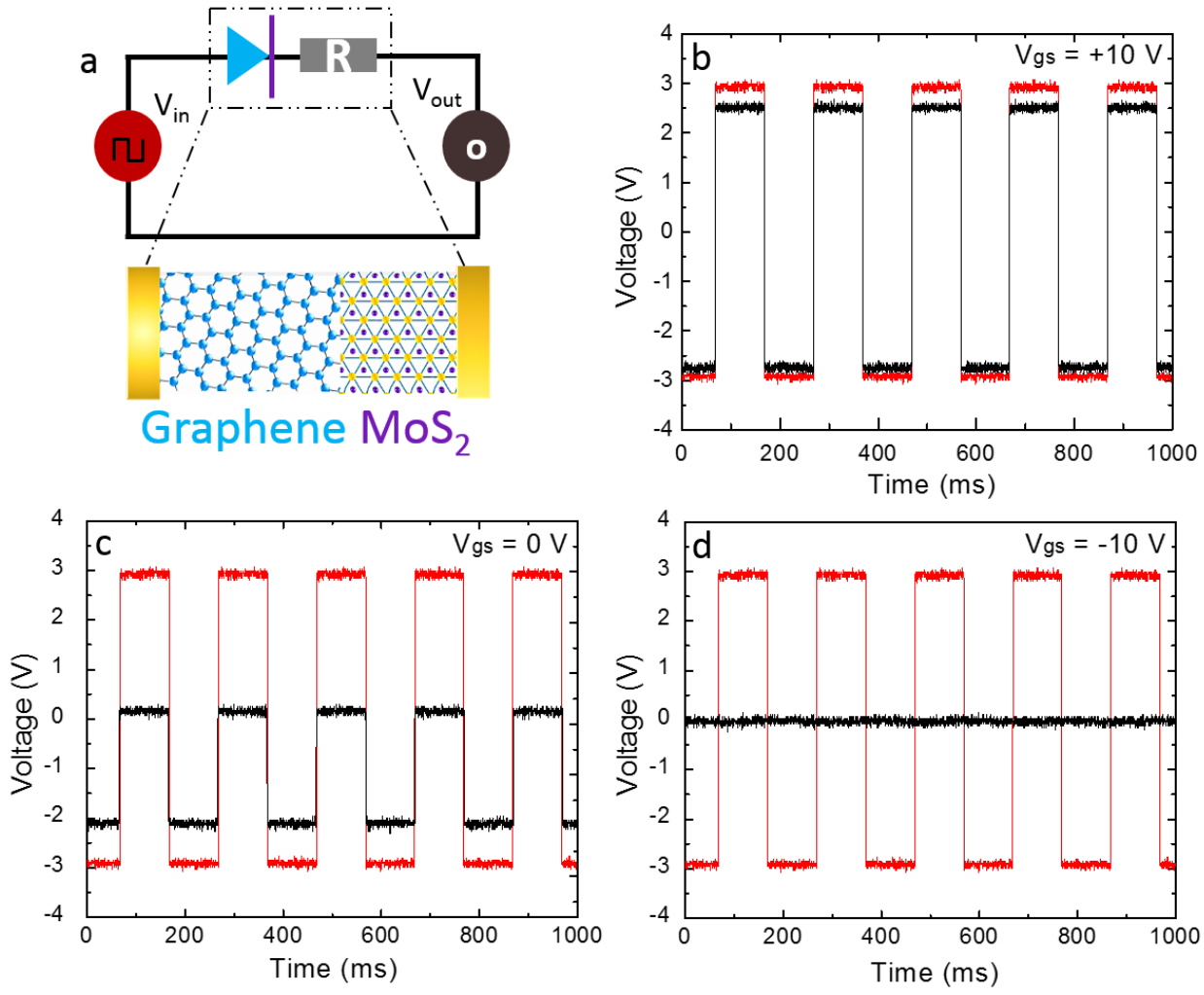

Figure. S10 (a) Schematic of the measurement set-up for rectifying square-wave input signal. The measurement were carried out at (b) positive (V_{gs} = + 10 V) (c) neutral (V_{gs} = 0 V) and (d) negative (V_{gs} = - 10 V) gate voltages. (The red curves indicate the input signal and the black curves show the output signal)

H. Device Fabrication, Raman Spectra of the device used for photo-analysis and its electrical hysteresis

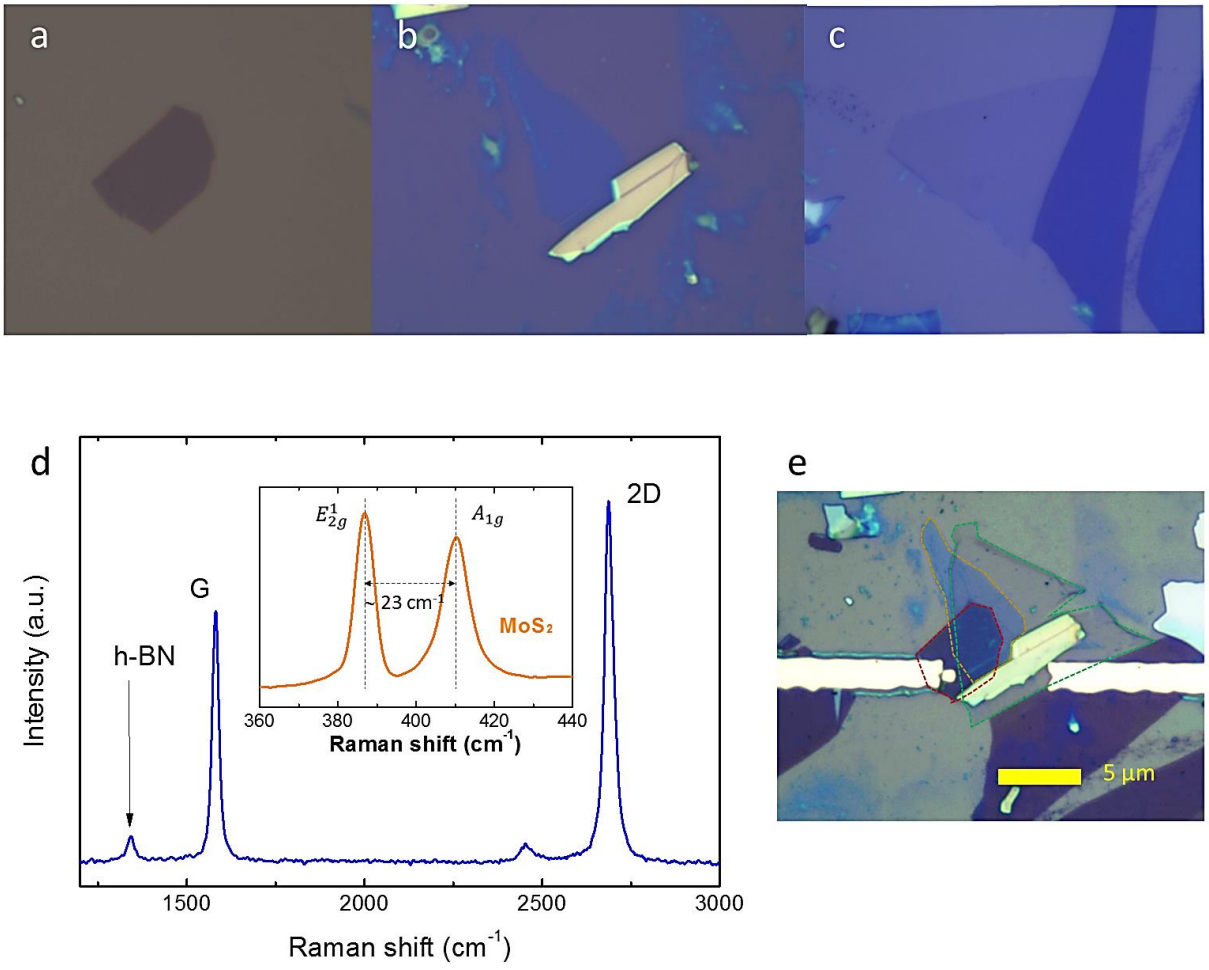

Figure S11. Optical Microscope image of the (a) multi-layer MoS_2 (b) few-layer h-BN (c) single graphene (d) Raman spectra of the respective layers, the typical peaks of single-layer graphene with the inset showing multi-layer (trilayer) MoS_2 spectra of showing 23 cm^{-1} approx. shift difference (e) optical image of the final fabricated device with connecting electrodes.

Figure S11 (a-e) shows the optical image of the individual layers before transfer, their Raman spectra and the image of the device after layer transfer and metal electrode deposition. It may be

noted that here the h-BN layer has no active role in the device electrical or optical characteristics and the single-layer graphene is in direct contact with the underlying few-layer MoS_2.

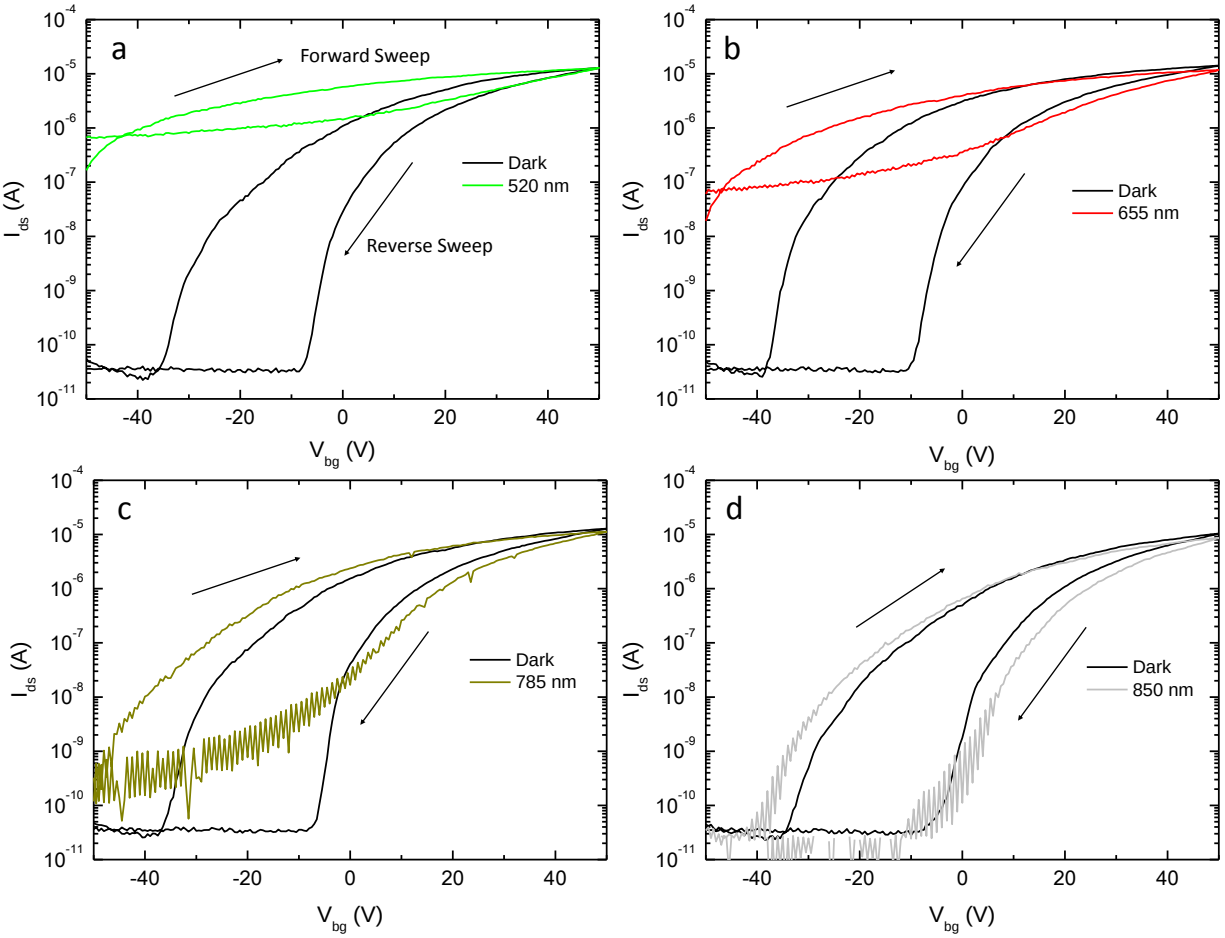

Figure. S12 Hysteresis characteristics of the graphene-MoS_2 hybrid sample. Hysteresis curves for dark and illuminated conditions in semi-log scale for (a-d) 520 nm, 655 nm, 785 and 850 nm wavelength, respectively.

Figure S12 (a –d) show the hysteresis behavior in the dark and laser of various wavelength in the semi-log scale. The hysteresis observed here is typical of MoS_2 devices, when measured in ambient atmosphere, due to traps and adsorbed gases like O_2 which captures electrons from the channel, thus behaves like negative charge ($O_2 + e^- = O_2^-$) and results in a right-shift of the

curve with lower threshold voltage due to electrons depletion in the channel.[16–18] As seen from the figures, the hysteresis area appears to be minimum for 520 nm wavelength and increases thereafter for 655, 785 and 850 nm. The dark and 850 nm hysteresis seems to be almost similar, with almost no shift in threshold voltage. Such dependence of hysteresis area on the laser wavelength could be due to the photo-activity of traps or impurities states and their energy and density distribution within the energy band gap.

I. References

(1) Das Sarma, S.; Adam, S.; Hwang, E. H.; Rossi, E. *Rev. Mod. Phys.* **2011**, *83*, 407–470.

(2) Late, D. J.; Liu, B.; Matte, H. S.; Dravid, V. P.; Rao, C. N. R. *ACS Nano* **2012**, *6*, 5635–5641.

(3) Li, T.; Du, G.; Zhang, B.; Zeng, Z. *Appl. Phys. Lett.* **2014**, *105*, 093107.

(4) Shih, C.; Wang, Q. H.; Son, Y.; Jin, Z.; Blankschtein, D.; Strano, M. S. *ACS Nano* **2014**, *8*, 5790-5798.

(5) Jariwala, D.; Sangwan, V. K.; Wu, C.-C.; Prabhumirashi, P. L.; Geier, M. L.; Marks, T. J.; Lauhon, L. J.; Hersam, M. C. *Proc. Natl. Acad. Sci. U. S. A.* **2013**, *110*, 18076–18080.

(6) Sutar, S.; Agnihotri, P.; Comfort, E.; Taniguchi, T.; Watanabe, K.; Ung Lee, J. *Appl. Phys. Lett.* **2014**, *104*, 122104.

(7) Fang, H.; Chuang, S.; Chang, T. C.; Takei, K.; Takahashi, T.; Javey, A. *Nano Lett.* **2012**, *12*, 3788–3792.

(8) Biswas, C.; Lee, S. Y.; Ly, T. H.; Ghosh, A.; Dang, Q. N. *ACS Nano* **2011**, *5*, 9817–9823.

(9) Cheiwchanchamnangij, T.; Lambrecht, W. R. L. *Phys. Rev. B - Condens. Matter Mater. Phys.* **2012**, *85*, 1–4.

(10) Mak, K. F.; He, K.; Lee, C.; Lee, G. H.; Hone, J.; Heinz, T. F.; Shan, J. *Nat. Mater.* **2013**, *12*, 207–211.

(11) Yu, L.; Lee, Y.-H.; Ling, X.; Santos, E. J. G.; Shin, Y. C.; Lin, Y.; Dubey, M.; Kaxiras, E.; Kong, J.; Wang, H.; Palacios, T. *Nano Lett.* **2014**, *14*, 3055–3063.

(12) Moriya, R.; Yamaguchi, T.; Inoue, Y.; Morikawa, S.; Sata, Y.; Masubuchi, S.; Moriya, R.; Yamaguchi, T.; Inoue, Y.; Morikawa, S.; Sata, Y. *Appl. Phys. Lett.* **2014**, *105*, *083119*.

(13) Kwak, J. Y.; Hwang, J.; Calderon, B.; Alsalman, H.; Munoz, N.; Schutter, B.; Spencer, M. G. *Nano Lett.* **2014,** *14*, 4511-4516.

(14) Lin, Y.-F.; Li, W.; Li, S.-L.; Xu, Y.; Aparecido-Ferreira, A.; Komatsu, K.; Sun, H.; Nakaharai, S.; Tsukagoshi, K. *Nanoscale* **2014**, *6*, 795–799.

(15) Lee, C.; Yan, H.; Brus, L. E.; Heinz, T. F.; Hone, J.; Ryu, S. *ACS Nano* **2010**, *4*, 2695–2700.

(16) Eckmann, A.; Felten, A.; Mishchenko, A.; Britnell, L.; Krupke, R.; Novoselov, K. S.; Casiraghi, C. *Nano Lett.* **2012**, *12*, 3925–3930.

(17) Ferrari, A. C.; Basko, D. M. *Nat. Nanotechnol.* **2013**, *8*, 235–246.

(18) Qiu, H.; Pan, L.; Yao, Z.; Li, J.; Shi, Y.; Wang, X. *Appl. Phys. Lett.* **2012**, *100*, 123104.